Optimizing UAV Hyperspectral Imaging for Urban Tree Chlorophyll and Leaf Area Index Retrieval

Shanshan Wei, Tiangang Yin, Bo Yuan, Kim Hwa Lim, Soo Chin Liew, and Andrew J. Whittle

***Abstract*—Uncrewed aerial vehicle (UAV) based hyperspectral imaging offers a flexible method for monitoring urban trees. However, its effect on estimating biochemical and biophysical parameters is still unknown. This article examines how spatial and spectral resolution, solar zenith angle (SZA), and diffuse solar irradiance (SKYL) affect chlorophyll content (C_{ab}) and leaf area index (LAI) estimation using narrow-band indices (NBIs) through three-dimensional radiative simulations. The results show that spatial resolution minimally affects C_{ab} estimation but significantly impacts LAI, with finer resolutions improving correlation with NBIs. In contrast, spectral resolution has little effect on LAI but greatly influences C_{ab}, with a 2-nm resolution providing stronger correlations, while resolutions coarser than 6 nm are less sensitive. The C_{ab} estimation prefers oblique SZAs, while LAI favors nadir SZAs. SKYL has little effect on C_{ab} and minor impact on LAI. Sunlit pixels outperform shaded ones for C_{ab} estimation, even at 2-m resolution, while entire-crown pixels show the highest LAI correlation. Different NBI strategies significantly affect LAI estimation but not C_{ab}. A consistent conclusion emerges from the analysis of correlations between UAV hyperspectral imagery, with varying spatial and spectral resolutions, and corresponding C_{ab} field measurements. This suggests that the knowledge revealed by the radiative transfer model is applicable to real-world conditions and improves understanding of natural processes without direct measurements.This article enhances the understanding of the influence of observation configurations on C_{ab} and LAI estimation, offering insights to optimize UAV-based hyperspectral imaging and guide future satellite sensor development for tree monitoring.**

***Index Terms*—Chlorophyll content (C_{ab}), hyperspectral remote sensing, leaf area index (LAI), uncrewed aerial vehicles (UAVs).**

Received 7 June 2024; revised 24 October 2024; accepted 31 October 2024. Date of publication 20 November 2024; date of current version 6 December 2024. The work of Tiangang Yin was supported by the Hong Kong Polytechnic University Faculty of Construction and Environment Start-up Fund (BE8W), and FCE Young Researcher Collaborative Research Fund (WZ82). This work was supported in part by the Singapore National Environment Agency under Grant CISR-2023-1R-19, in part by the research project "Computerised Management of Urban Trees: Tree Inspection Using Satellite Data" funded by the National Parks Board of Singapore (2017–2021) and conducted through the SMART Center for Environmental Modeling and Sensing. *(Corresponding author: Tiangang Yin.)*

Shanshan Wei, Kim Hwa Lim, and Soo Chin Liew are with the Centre for Remote Imaging, Sensing and Processing, National University of Singapore, Singapore 119076 (e-mail: weiss526@gmail.com; crskhl@nus.edu.sg; scliew@nus.edu.sg).

Tiangang Yin is with the Department of Land Surveying and Geo-Informatics, The Hong Kong Polytechnic University, Hong Kong (e-mail: tiangang.yin.85@gmail.com).

Bo Yuan is with the School of Information Engineering, Zhejiang Ocean University, Zhoushan 316022, China (e-mail: yuanbo@u.nus.edu).

Andrew J. Whittle is with the Department of Civil and Environmental Engineering, Massachusetts Institute of Technology, Cambridge, MA 02139 USA (e-mail: ajwhittl@mit.edu).

Digital Object Identifier 10.1109/JSTARS.2024.3498900

I. Introduction

URBAN trees are essential for promoting urban biodiversity, advancing environmental sustainability, and enhancing climate resilience. They provide a variety of ecosystem services, including enhancing thermal comfort [1], mitigating air and noise pollution [2], sequestering carbon [3], and managing stormwater [4]. However, structural failures of unhealthy trees can present a danger to people and property. Monitoring the health of urban trees can reduce these risks, but currently involves a labor-intensive process relying on human inspection.

Remote sensing offers a more efficient solution for tree monitoring. Two key plant traits, chlorophyll content (C_{ab}) and leaf area index (LAI), are commonly quantified for plant health monitoring [5], [6], [7], [8], [9], [10], [11], [12], [13]. The rapid advancements in imaging spectroscopy and uncrewed aerial vehicle (UAV) provide enhanced flexibility in both spatial and spectral resolutions, enabling data capture under various solar zenith angles (SZAs), and diffuse ratios of solar irradiance (SKYL). However, notable gaps exist in understanding how these flexibilities of UAV configurations influence the retrieval of canopy C_{ab} and LAI.

Higher spatial resolutions enable detailed inspection of individual trees but reduce flight efficiency. Some studies prefer higher spatial resolution images and a resolution finer than 4 cm has been recommended for optimal C_{ab} estimation in sugar beet crops [14]. Additionally, higher spatial resolution images are beneficial for improving LAI estimation [15]. Conversely, other studies suggest that coarse spatial resolution can perform similarly to high spatial resolution at a lower cost [16], [17]. These differing opinions underscore the need to examine the influence of spatial resolution on tree C_{ab} and LAI estimation and to determine the optimal resolution for these parameters.

Hyperspectral images are typically believed to enhance the detection of subtle spectral variations related to plant traits, with narrow-band indices (NBIs) outperforming multispectral images for C_{ab} and LAI estimation [18], [19], [20], [21], [22], [23], [24], [25], [26]. Nevertheless, higher spectral resolutions may increase the costs of data acquisition, processing, and retrieval. Hence, determining the optimal spectral resolution for C_{ab} and LAI estimation is crucial for advancing UAV applications.

Previous UAV images were commonly acquired around noon with an SZA close to nadir [27], [28], [29], [30], [31], to increase the proportion of sunlit leaves [28], [29]. The sunlit leaves demonstrated an advantage for C_{ab} estimation [13], [34], [35], [36]. However, the nadir SZA also amplifies the background's influence by increasing the proportion of sunlit background. Urban tree spectra are particularly susceptible to contamination

by background with high diversity and spectral complexity [11], [37], [38], [39]. Sunlit background may exacerbate this influence. Specific observation times (e.g., 15:00 h) with oblique SZAs have been proposed to mitigate background influence for wheat row crops [33]. However, the background of urban trees differs significantly from that of row crops. Thus, the optimal SZAs for C_{ab} and LAI estimation for urban trees remain unknown.

Hyperspectral images captured under clear sky conditions are usually used for C_{ab} and LAI estimation even though UAVs can capture hyperspectral images under diverse illumination conditions [34]. Recent studies showed that even under the lowest overall irradiance with the thickest cloud cover, the signal-to-noise ratio (SNR) of hyperspectral images is adequate for retrieving foliar traits [35]. Moreover, recent studies have demonstrated the usability of hyperspectral images acquired during varying illumination and cloudy conditions for C_{ab} estimation [36]. However, there is a lack of studies exploring the influence of SKYL to the C_{ab} and LAI estimation.

This article aims to identify the optimal observation configurations for estimating the C_{ab} and LAI of urban trees using hyperspectral images. We focus on two significant aspects that influence C_{ab} and LAI estimation with hyperspectral imaging: 1) sensor settings, including spatial and spectral resolutions, and 2) illumination conditions, including SZA and diffuse ratio. This article is significant not only for estimating vegetation parameters using UAV-based instruments but also for providing valuable insights into appropriate spatial and spectral resolution selection for upcoming satellite missions.

II. Data and Methods

Given the challenges in obtaining extensive reliable field measurements (for C_{ab} and LAI) and expenses involved in deploying UAVs to acquire hyperspectral images with diverse spatial/spectral resolutions under different SZA and SKYL conditions, this article utilized a modeling framework. This modeling framework simulates hyperspectral data for realistic trees to evaluate the impact of observation configurations on C_{ab} and LAI estimation. Here, we use the PROSPECT-5 model [37], [38] integrated with discrete anisotropic radiative transfer (DART) model [45], [46], [47], [48] to simulate UAV hyperspectral images of urban trees.

A. Hyperspectral Images Simulation

The DART scene dimensions were set to 40 m × 40 m, with an individual three-dimensional (3-D) tree model positioned at the scene center. Details about the 3-D tree model are provided in [43]. The DART scene incorporated six different backgrounds, including dry soil, wet soil, sand, grass, concrete, and asphalt, to reflect the complex backgrounds of urban trees. The optical properties of these backgrounds were randomly chosen from the urban background spectral database [36]. For grass backgrounds, the LAI of the grass was assigned a random value between 0 and 1. The leaf spectral properties were simulated by PROSPECT with variable input parameters suitable for trees. The SZA was set to 0°, 15°, 30°, and 45° that correspond to nadir and oblique directions. The view zenith angle (VZA) was set to 0° to represent the nadir view for most UAV-based observations. The SKYL was set to 0, 0.2, 0.4, 0.8, and 1.0, with 0 being direct illumination and 1 being fully overcast. The input parameters of the simulation are described in Table I.

TABLE I
Simulation Parameter Variation for the NBIs Selection

	Parameters	Min	Max	Mean	Std
Leaf scale	Brown pigment	0	0.2	0	0.1
	Chlorophyll (μg cm^{-2})	10	80	40	30
	Structure coefficient	1.5	2.5	1.9	0.4
	Equivalent water thickness (μg cm^{-2})	0.002	0.042	0.015	0.01
	Leaf mass per area (g cm^{-2})	0.002	0.033	0.008	0.01
	Anthocyanin (μg cm^{-2})	0	4	2	2
Canopy scale	Leaf percentage	100%, 50% , and 10%			
Illumination condition	SKYL	0, 0.2, 0.4, 0.6, 0.8, 1			
	SZA (°)	0°, 15°, 30°, 45°			
Background	Reflectance property	Dry soil, wet soil, grass, asphalt, concrete, and sand			

To explore the influences of spatial resolution on C_{ab} and LAI estimation, the spatial resolution was set to 0.1, 0.5, 1.0, and 2.0 m for each type of background. Similarly, the spectral resolution was set to 2, 6, 10, and 14 nm for wavelenths spanning from 400 to 1000 nm to explore the influence of spectral resolution on C_{ab} and LAI estimation. The resultant images from DART simulations were applied with 5% random multiplicative noise to mimic realistic situations. In total, 69 120 (720 × 6 × 4 × 4) hyperspectral images were simulated for subsequent NBIs evaluations for C_{ab} and LAI estimation.

Observation configurations can affect the reflectance distribution of simulated image pixels and the overall reflectance spectrum, as illustrated by selected examples from the simulated datasets in Fig. 1. A spatial resolution of 0.1 m preserves details of a tree. In comparison, a lower resolution of 2 m blurs the same tree, yet sunlit and shaded pixels of its crown remain visible [Fig. 1(a)]. As the SKYL increases, the contrast between sunlit and shaded pixels decreases, with shadows almost vanishing at a SKYL value of 1.0 [Fig. 1(b)]. The proportion of shaded leaves increases with more oblique SZA values [Fig. 1(c)]. Additionally, hyperspectral images with a spectral resolution of 2 nm capture detailed canopy responses with dense narrow bands, while a lower spectral resolution of 16 nm results in much sparser observations, particularly in the 700 to 780 nm red-edge region [Fig. 1(d)].

B. UAV Hyperspectral Images Aquisition

Two hyperspectral UAV flight campaigns were conducted over Bishan-Ang Mo Kio Park, Singapore (Lat: 1.363°, Long: 103.845°) on 10 October 2020 and on 27 February 2021

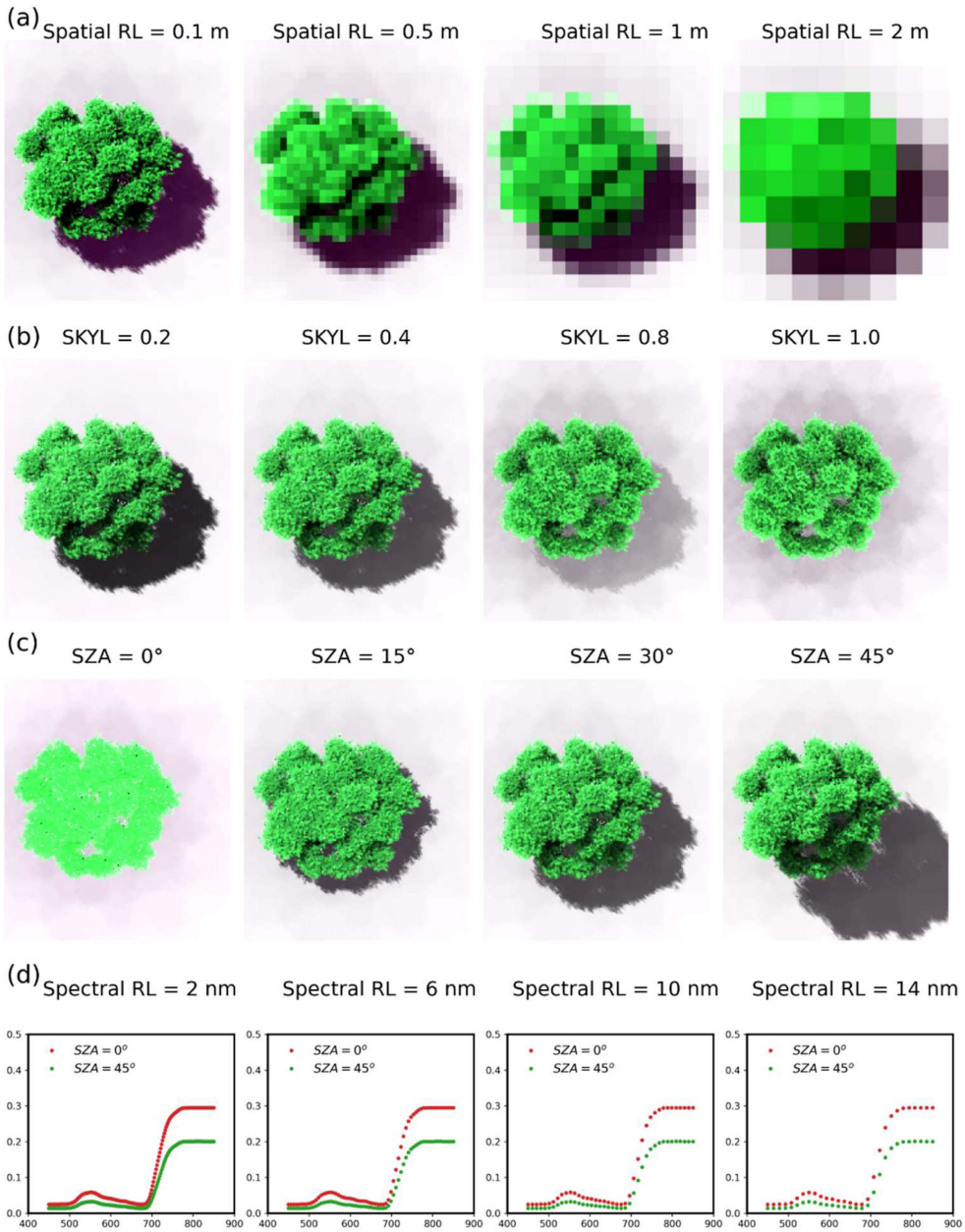

Fig. 1. Simulated hyperspectral images with varying (a) spatial resolutions (RL), (b) diffuse ratio of solar irradiance (SKYL), (c) solar zenith angles (SZAs), and (d) resultant scene reflectance spectra at different spectral resolutions.

(Fig. S1), using a Headwall Nano-Hyperspec push-broom imager mounted on a DJI Matrice 600 Pro quadcopter. Detailed on image acquisition and processing is provided in [36].

Similar to the simulated images, the performance of C_{ab} estimation was evaluated across varying spatial/spectral resolutions. The original 0.1-m spatial resolution was degraded to 0.5, 1, and 2 m by averaging over cells of $N \times N$ pixels, resulting in four sets of hyperspectral images with different spatial resolutions. Similarly, the original spectral resolution of 2 nm was degraded to 6, 10, and 14 nm by averaging in the spectral dimension.

C. C_{ab} Field Measurement

C_{ab} field measurements were conducted on 20 October 2020 and 8 March 2021. The C_{ab} of 60 leaves from each tree crown was measured using an SPAD-502 chlorophyll meter. Detailed measurement procedures and the calibrated C_{ab} values (μg cm^{-2}) for each tree are provided in [36].

D. Sunlit/Shaded Pixels Classification

The tree crowns were manually delineated and used as crown masks from the simulated hyperspectral images. Subsequently, these delineated crown pixels underwent classification into five categories: sunlit, shaded, bright (specular reflection), dark (cavities within the leaves), and background, using an automated crown classification method [36]. Fig. 2 shows the example of simulated hyperspectral images of a tree crown (*Peltophorum pterocarpum*) with varying spatial resolutions, and the results of delineation and classification. The polygon of a delineated

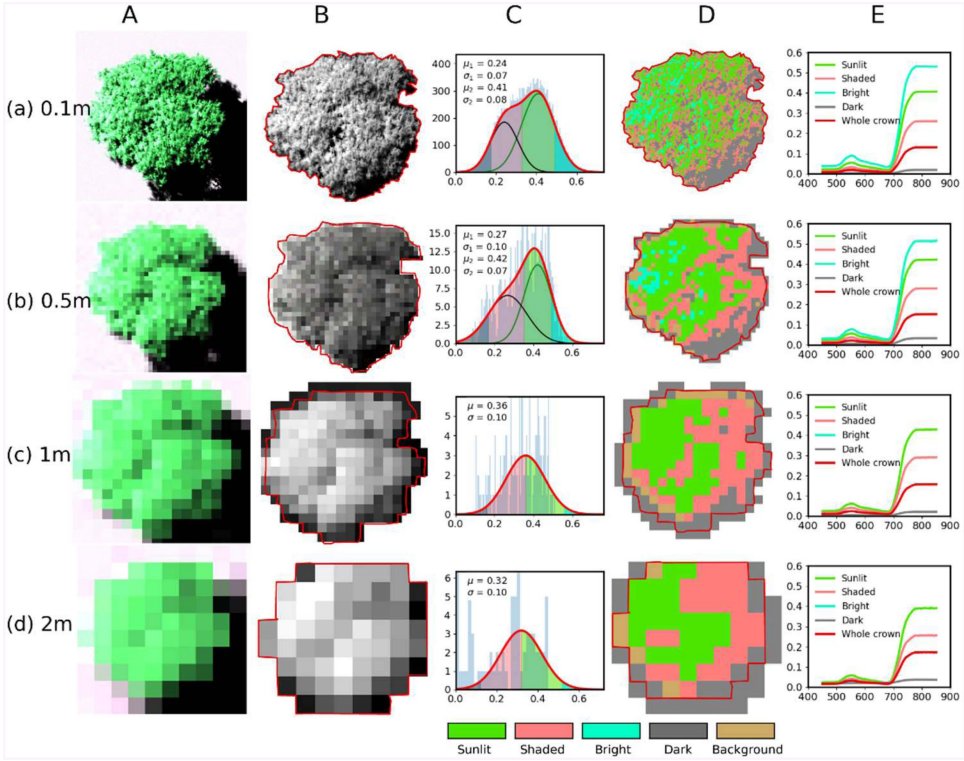

Fig. 2. Automatic classification of tree crown pixels using simulated images with different spatial resolutions: (A) delineated tree crown on the RGB composition (R: 660.0 nm, G: 551.0 nm, and B: 459.9 nm); (B) corresponding tree crown on the NIR band (850 nm); (C) NIR histogram curve and Gaussian fitting for classification; (D) tree crown classification results; and (E) average reflectance spectrum of different crown classes.

crown becomes simpler as the spatial resolution decreases from 0.1 to 2.0 m [Fig. 2(a) and (b)]. The histogram of the NIR band (851 nm) degrades from a bimodal to a monomodal Gaussian distribution as the resolution decreases [Fig. 2(c)]. As spatial resolutions become coarser, the pixels classified as sunlit and shaded begin to merge. At a 2-m resolution [Fig. 2(d)], more pixels at the edge of the crown are classified as shaded or background due to the mixing effect. A significant difference between sunlit and shaded reflectance can be observed at all spatial resolutions [Fig. 2(e)]. The same automatic sunlit/shaded classification method was applied to the UAV hyperspectral images at different spatial resolutions (Fig. 3).

E. Index Computation Formulations and Strategies

Although deep learning has demonstrated significant potential and effectiveness in vegetation monitoring [44], [45], index-based methods are more commonly used due to their ease of implementation in remote sensing applications. In this article, we focus on exploring the influence of UAV configuration on C_{ab} and LAI estimation by scanning across a range of NBIs method. The NBIs are commonly expressed as ratios of reflectance values in two or three spectral bands, using the following three formats:

1) Simple ratio (SR)

$$\mathrm{SR} = \frac{\rho_{\lambda 1}}{\rho_{\lambda 2}}. \tag{1}$$

2) Normalized difference ratios (mND)

$$\mathrm{mND} = \frac{(\rho_{\mathrm{ref}} - \rho_{\lambda 1})}{(\rho_{\mathrm{ref}} + \rho_{\lambda 2})}. \tag{2}$$

3) Structure-insensitive pigment index (SIPI)

$$\mathrm{SIPI} = \frac{(\rho_{\mathrm{ref}} - \rho_{\lambda 1})}{(\rho_{\mathrm{ref}} - \rho_{\lambda 2})} \tag{3}$$

where λ_1, λ_2, and λ_{ref} denote the variable bands and the reference band, respectively. Previous evaluations have typically focused on a limited number of NBIs [46], [47]. This article evaluates all potential indices by varying λ_1, λ_2, and λ_{ref} from 450 to 851 nm, with an average bandwidth of 6.6 nm for simulation data and 2 nm for UAV hyperspectral data. Given that mND and SIPI have demonstrated better performance than SR in previous articles, this article focuses on the mND and SIPI formulations [36].

Two index calculation strategies for determining NBIs from crown pixels were evaluated for their impact on the C_{ab} and LAI estimation as follows:

1) computing NBIs from the average reflectance of all crown pixels (Ref_AVG), and
2) determining the average NBIs for each individual pixel within the crown (Index_AVG).

The correlations between these NBIs and both C_{ab} and LAI were investigated for their sensitivity to different crown sections, including sunlit, shaded, and the entire crown. Subsequently, the correlations between these NBIs and both C_{ab} and LAI were analyzed for their sensitivity to UAV sensor configurations (spatial and spectral resolutions) and environmental conditions (SZA and SKYL). The maximum Spearman's rank correlation coefficient between NBIs (calculated for all combinations of λ_1 and λ_2 over various λ_{ref}) and both C_{ab} and LAI across different

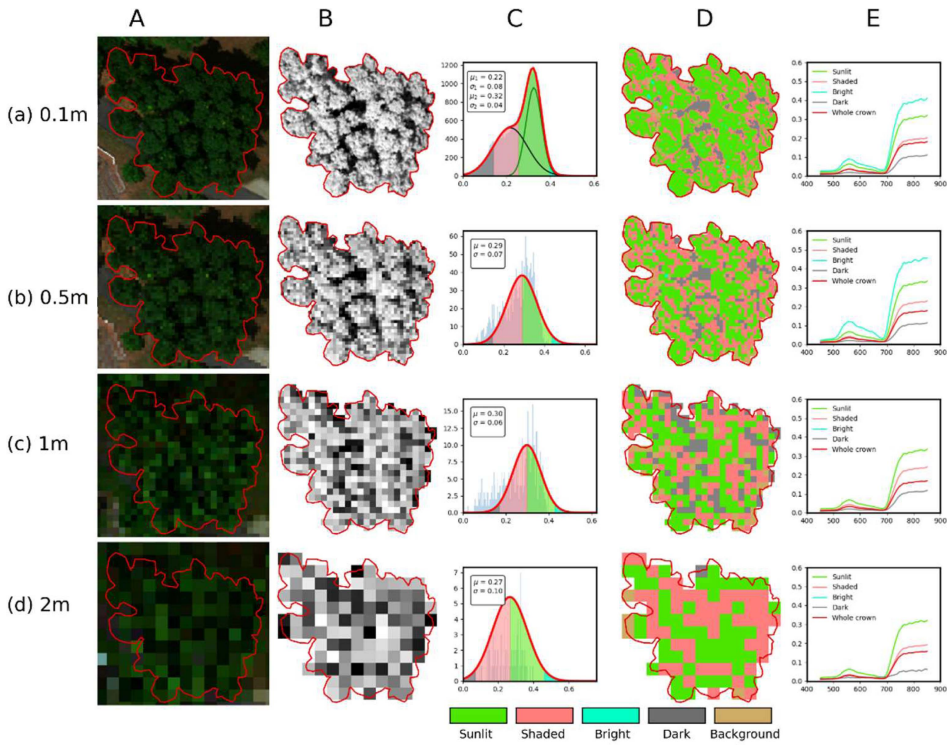

Fig. 3. Automated classification of tree crown pixels using UAV hyperspectral images at different spatial resolutions: (a) 0.1 m, (b) 0.5 m, (c) 1 m, and (d) 2 m.

spatial resolutions (0.1, 0.5, 1.0, and 2.0 m) were compared to assess the impact of spatial resolution on the estimation of C_{ab} and LAI. Similarly, various spectral resolutions, including 2, 6, 10, and 14 nm, were examined to assess their effect on the estimation of C_{ab} and LAI. In addition, we further evaluate the impacts of four selected SZAs (SZA $= 0°$, $15°$, $30°$, and $45°$); and three ranges of diffuse ratio: 1) $0 <$ SKYL < 0.2 (direct dominant illumination), 2) $0.4 <$ SKYL < 0.6 (partially cloudy illumination); and 3) $0.8 <$ SKYL < 1 (diffuse dominant illumination) on the correlation between NBIs and both C_{ab} and LAI.

III. Results

A. Pixel Selection and Index Calculation Strategy From Simulation Data

The pixel selection and index calculation strategy can strongly influence the estimation of C_{ab} and LAI, as demonstrated by the heatmap of correlation as a function of λ_1 and λ_2 wavebands with corresponding wavelengths bands (λ_{ref}) in the subplot, and the maximum correlation between NBIs and both C_{ab} and LAI across various reference wavelengths (λ_{ref}) in Fig. 4. For C_{ab} estimation, sunlit pixels exhibit a higher maximum correlation with NBIs compared to shaded and entire-crown pixels for both index calculation strategies (Index_AVG and Ref_AVG) [Fig. 4(a) and (b)]. Conversely, LAI estimation showed significant differences in crown pixel selection when using the two index calculation strategies [Fig. 4(c) and (d)]. Using the Ref_AVG strategy, the largest maximum correlation for LAI was achieved with $SIPI_{\lambda_{ref}}$ $[\lambda_1, \lambda_2]$, where λ_{ref} is larger than 700 nm, utilizing sunlit or entire-crown pixels. With the Index_AVG strategy, the largest maximum correlation was obtained with $SIPI_{\lambda_{ref}}$ $[\lambda_1, \lambda_2]$ where λ_{ref} ranges from 450 to 500 nm using entire-crown pixels. Overall, the highest correlation between LAI and NBIs is attained using the entire-crown pixel for both index calculation strategies. Based on these findings, sunlit pixels were selected for C_{ab} analysis, while entire-crown pixels were used for LAI analysis in the subsequent sections.

B. Sensor Configuration From Simulation Data

The spatial resolution can influence the correlation between NBIs and both C_{ab} and LAI in various ways (Fig. 5). The correlation between NBIs and C_{ab} decreases slightly with spatial resolution dropping from 0.1 to 0.5 m and 1 m. However, at 2-m spatial resolution, the correlation between NBIs and C_{ab} decreases significantly compared to 1-m resolutions [Fig. 5(a) and (b)]. The influence of spatial resolution on the correlation between LAI and NBIs is more pronounced than for C_{ab} [Fig. 5(c) and (d)]. Finer spatial resolution exhibits a notably higher correlation than coarser spatial resolution for LAI estimation for both SIPI and mND and both index calculation strategies. Specifically, the 0.1-m resolution demonstrates clear superiority in correlation over the 0.5 m and the 0.5-m resolution consistently displays higher correlations than the 1.0-m resolution. Likewise, the 1.0-m resolution outperforms the 2.0-m resolution across all reference bands.

The spatial resolutions also impact the correlation distribution pattern between NBIs and C_{ab}, as well as LAI (Fig. 6), utilizing the optimal index format, reference band, and index calculation strategy determined from the evaluation results in Fig. 4. Specifically, $SIPI_{\lambda_{ref}}$ $[\lambda_1, \lambda_2]$ with $\lambda_{ref} = 711$ nm was chosen for both index calculation strategies for C_{ab} estimation,

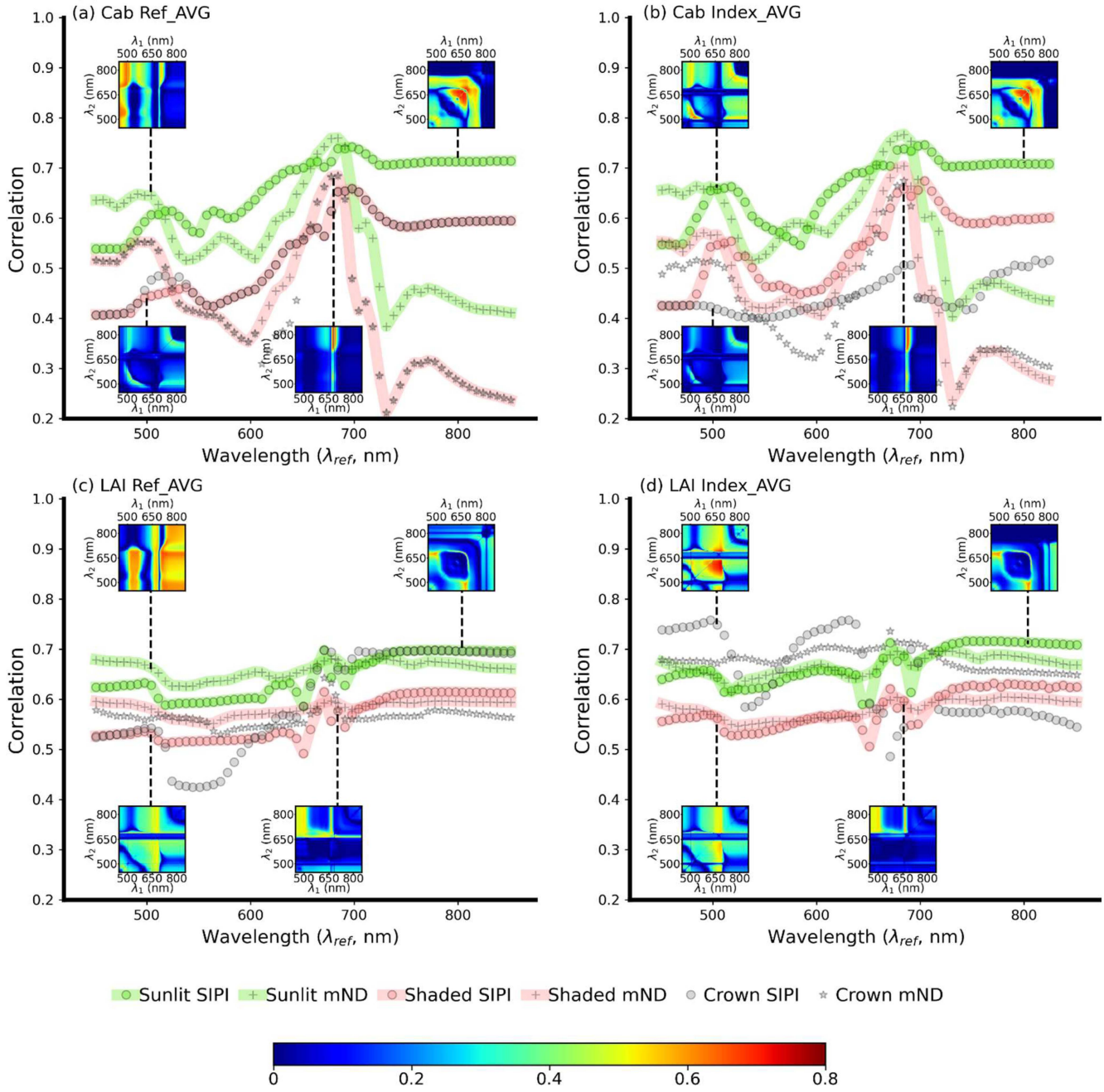

Fig. 4. Maximum Spearman's correlation coefficient values between NBIs and (a and b) C_{ab} and (c and d) LAI using various reference bands (λ_{ref}) in the $SIPI_{\lambda_{ref}}$ [λ_1, λ_2], and $mND_{\lambda_{ref}}$ [λ_1, λ_2] format from sunlit, shaded, and entire-crown pixels at 0.1-m spatial resolution. (a and c) Ref_AVG strategy. (b and d) Index_AVG strategy. The subfigure demonstrates the heat map of squared Spearman's correlation as a function of λ_1 and λ_2 wavebands with corresponding reference bands.

while $SIPI_{\lambda_{ref}}$ [λ_1, λ_2] with $\lambda_{ref} = 800$ nm for Ref_AVG strategy, with $\lambda_{ref} = 490$ nm for Index_AVG strategy for LAI estimation. The correlation distribution pattern between $SIPI_{\lambda_{711}}$[λ_1, λ_2] and C_{ab} is not influenced by the index calculation strategy or spatial resolution [Figs. 6(a) and (b)]. High correlation regions are observed when λ_1 ranges from 700 to 850 nm and λ_2 ranges from 650 to 700 nm, along with another high correlation region encompassing both λ_1 and λ_2 from 600 to 650 nm, and a third high region with λ_1 and λ_2 from 650 to 700 nm. In contrast, the impact of spatial resolution on LAI estimation varies depending on the index calculation strategy and spatial resolution [Fig. 6(c) and (d)]. With the Ref_AVG strategy, the highest correlation between $SIPI_{\lambda_{800}}$ and LAI is achieved by selecting both λ_1 and λ_2 from 650 to 700 nm. Conversely, using the Index_AVG strategy, the maximum correlation between $SIPI_{\lambda_{490}}$ and LAI is attained by choosing λ_1 from 650 to 700 nm and λ_2 from 650 to 800 nm. The correlation between LAI and NBIs decreases with coarser spatial resolutions, especially when utilizing entire-crown pixels for both index calculation strategies. Sunlit pixels are less affected by spatial resolution. Specifically, the effectiveness of entire-crown pixels over sunlit pixels diminishes with coarser spatial resolutions until sunlit pixels outperform

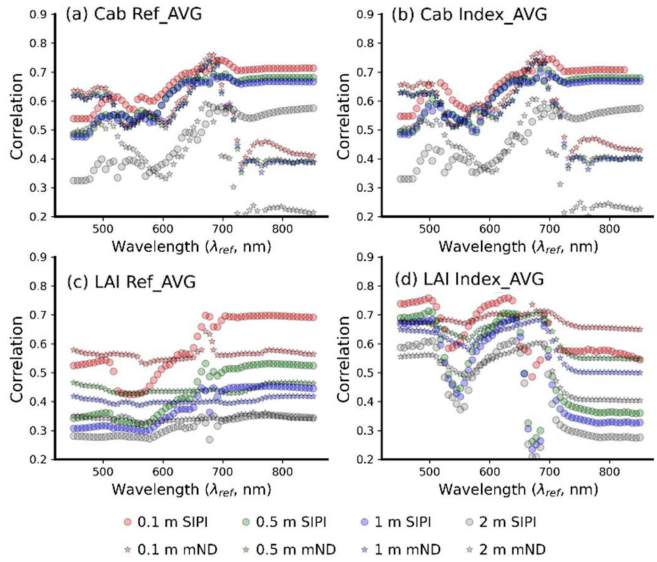

Fig. 5. Maximum Spearman's correlation coefficient values between NBIs and (a and b) C_{ab} and (c and d) LAI, utilizing various reference bands (λ_{ref}) in the $SIPI_{\lambda_{ref}}$ [λ_1, λ_2] and $mND_{\lambda_{ref}}$ [λ_1, λ_2] format, with different spatial resolutions (0.1, 0.5, 1, and 2 m). Panels (a and c) use Ref_AVG strategy, while panels (b and d) use the Index_AVG strategy. The spectral resolution employed is 2 nm.

using entire crown pixels when the spatial resolution deteriorates to 2 m.

1) Spectral Resolution: The influence of the spectral resolution on C_{ab} [Fig. 7(a) and (b)] estimation using NBIs is larger than that for LAI [Fig. 7(c) and (d)]. For C_{ab}, SIPI with a 2-nm spectral resolution shows significantly higher correlation than other coarser spectral resolutions for most of the reference bands (λ_{ref}). In contrast, the 6, 10, and 14 nm spectral resolutions exhibit similar correlations across all reference band. Conversely, mND is relatively insensitive to spectral resolution, showing little variation across all reference bands for different spectral resolutions. For LAI, the influence of spectral resolution on the correlation with NBIs depends on the index calculation strategy. For the Ref_AVG strategy [Fig. 7(c)], SIPI exhibits a noticeably higher correlation with LAI for finer spectral resolutions, while spectral resolution has minimal impact on mND. When using the Index_AVG strategy [Fig. 7(d)], spectral resolution has mnimal impact on LAI estimation for both SIPI and mND format NBIs.

C. Illumination Configuration From Simulation Data

1) Solar Zenith Angle (SZA): The SZA shows a significant influence on the maximum correlation between NBIs and both C_{ab} and LAI (Fig. 8). For C_{ab}, the correlation between C_{ab} and NBIs in the SIPI format increases with SZA, with the highest correlation observed at SZA $= 45°$ and the lowest at SZA $= 0°$, across almost all reference wavelength [Fig.8(a) and (b)]. This suggests that C_{ab} estimation using SIPI is more accurate when using oblique SZA angles. The SZA seems to have less influence on the correlation between C_{ab} and mND. In contrast, the correlation between LAI and NBIs decreases as SZA increases, with the highest correlation observed at SZA $= 0°$ and the lowest at SZA $= 45°$ for both SIPI and mND using both index calculation strategies [Fig.8(c) and (d)]. This indicates that LAI estimation based on NBIs performs better when the SZA is closer to the nadir angle. Comparing the two index calculation strategies, Index_AVG is more sensitive to SZA, with SZA $= 0°$ providing a significant advantage over oblique SZAs (15°, 30°, and 45°).

2) Diffuse Ratio of Solar Irradiance (SKYL): The SKYL shows a small influence on the correlation between NBIs and both C_{ab} and LAI (Fig. 9). Regarding C_{ab}, direct dominant illumination ($0 <$ SKYL < 0.2) slightly outperforms other illuminations over the reference wavelength range between 650 and 750 nm. However, the influence of SKYL on C_{ab} becomes negligible when other reference bands are used in the NBIs [Fig. 9(a) and (b)]. The impact of SKYL on the correlation between NBIs and LAI is relatively larger and dependent on the chosen index calculation strategy [Fig. 9(c) and (d)]. Using the Ref_AVG calculation strategy, direct dominant illumination exhibits a slightly higher correlation than other illuminations across all reference bands for both SIPI and mND. On the other hand, under the Index_AVG calculation strategy, diffuse dominant illumination demonstrates a higher correlation compared to direct dominant illumination, particularly for the mND.

D. Pixel Selection and Index Calculation Strategy From UAV Hyperspectral Images

For the correlation between NBIs derived from UAV hyperspectral images and field C_{ab}, sunlit pixels show a higher maximum correlation with NBIs, compared to shaded and entire-crown pixels for both index calculation methods [Fig. 10(a) and (b)]. The $SIPI_{\lambda_{ref}}$ [λ_1, λ_2] and $mND_{\lambda_{ref}}$ [λ_1, λ_2] profiles across different reference bands are nearly identical for both strategies, indicating that the choice of calculation method does not impact C_{ab} estimation using NBIs, consistent with the simulation results (Fig. 4).

E. Sensor Configuration From UAV Hyperspectral Images

For NBIs derived from UAV hyperspectral images, the 0.1-m resolution consistently shows the strongest correlation with field-measured C_{ab} across all reference bands, outperforming the 0.5, 1, and 2 m resolutions for both NBI types ($SIPI_{\lambda_{ref}}$ [λ_1, λ_2] and $mND_{\lambda_{ref}}$ [λ_1, λ_2]), using both calculation strategies (Ref_AVG and Index_AVG strategy) (Fig. 11). The correlation between NBIs and C_{ab} declines noticeably as spatial resolution decreases from 0.1 to 0.5, 1, and 2 m, which is consistent with simulation results (Fig. 5).

The substantial differences in the maximum correlation coefficient values between NBIs derived from UAV hyperspectral images and C_{ab} across various spectral resolutions (2, 6, 10, and 14 nm) indicate that spectral resolution significantly influences C_{ab} estimation (Fig. 12). Specifically, the SIPI with a 2-nm spectral resolution exhibits a markedly higher correlation than the coarser spectral resolutions for most reference bands (λ_ref). In contrast, the differences among the 6, 10, and 14 nm spectral resolutions are less pronounced than those observed with the 2-nm resolution, although the 6-nm resolution consistently outperforms both the 10 and 14 nm resolutions across all reference bands. This is consistent with the spectral resolution influence results using simulation data (Fig. 7).

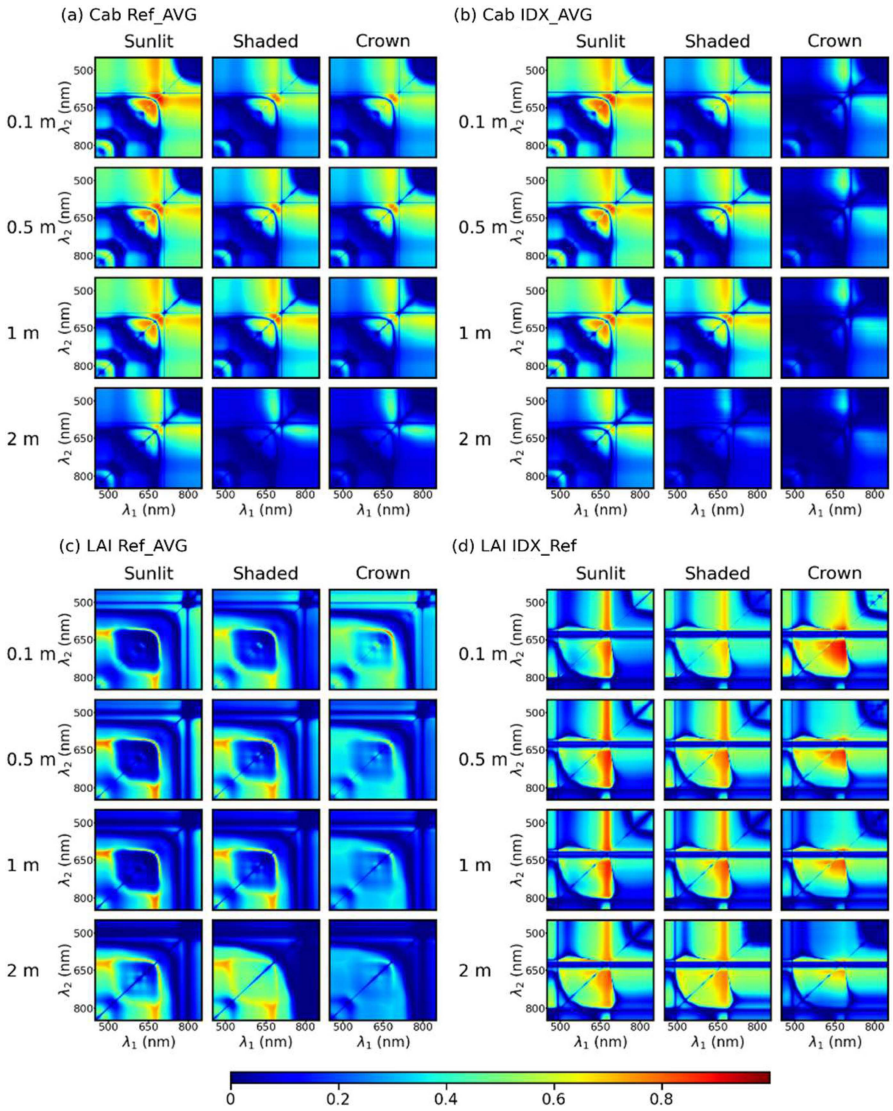

Fig. 6. Heatmap of squared Spearman's correlation: between $SIPI_{\lambda_{711}}$ [λ_1, λ_2] and C_{ab} using (a) Ref_AVG and (b) Index_AVG, and (c) between $SIPI_{\lambda_{800}}$ [λ_1, λ_2] and LAI using Ref_AVG, (d) between $SIPI_{\lambda_{490}}$ [λ_1, λ_2] and LAI using Index_AVG, as a function of λ_1 and $\lambda 2$ wavebands, with corresponding reference bands for sunlit, shaded, and crown.

IV. Discussion

A. Pixel Selection and Index Calculation Strategy

One advantage of high spatial resolution images is the ability to select sensitive pixels for better C_{ab} and LAI estimation. Sunlit and shaded classification is commonly used for C_{ab} and LAI estimation using images with submeter resolutions. Coarser than this resolution, the differences between sunlit and shaded pixels are often ignored [34], [48], [49]. However, this article reveals substantial differences in reflectance between sunlit and shaded pixels even in images with 2-m spatial resolution [Fig. 2(d)]. In addition, the article demonstrates that the correlation between NBIs and C_{ab} exhibits significant differences between sunlit and shaded pixels for images with 1 and 2 m spatial resolutions. Inferior performance was demonstrated when using the entire crown without distinguishing between the sunlit and the shaded pixels for C_{ab} (Fig. 6). This underscores the importance of sunlit and shaded pixel classification, even in 2-m spatial resolution imagery. This finding may seem contradictory to another urban tree study using 2-m spatial resolution hyperspectral images [11], which found that using sunlit pixels did not improve index correlation for C_{ab}. This discrepancy may be due to their usage of a threshold classification method, which may not be suitable for classifying sunlit and shaded areas of urban trees because of their heterogeneous and complex nature. To address this issue, a method based on statistical theory proposed in our prior research for urban tree sunlit and shaded pixel classification [36] has been adopted here. Previous articles excluded pixels intersecting with the tree crown border to mitigate contamination from background materials [11]. This aligns with our findings that pixels at the crown border are predominantly composed of mixed pixels at 2-m spatial resolution [Fig. 2(d)].

This article shows that sunlit pixels have a significant advantage over shaded pixels and entire-crown pixels for estimating C_{ab} (Fig. 4). This finding is consistent with previous research, as sunlit pixels can enhance the SNR and minimize background

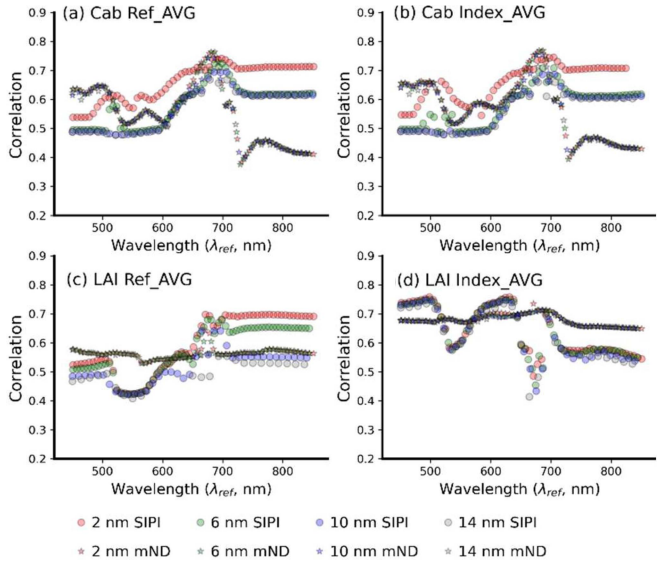

Fig. 7. Maximum Spearman's correlation coefficient values between NBIs and (a and b) C_{ab}, as well as (c and d) LAI, for different spectral resolutions (2, 6, 10, and 14 nm) using various reference bands (λ_{ref}) in the $SIPI_{\lambda_{ref}}$ [λ_1, λ_2] and $mND_{\lambda_{ref}}$ [λ_1, λ_2] format. In (a and c), the index calculation strategy is Ref_AVG. In (b and d), the index calculation strategy is Index_AVG. The spatial resolution utilized was 0.1 m.

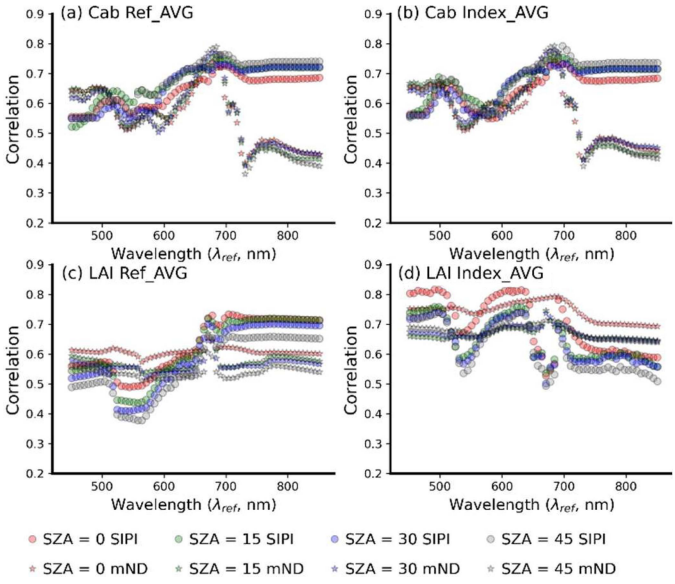

Fig. 8. Maximum Spearman's correlation coefficient values between NBIs and (a and b) C_{ab}, as well as (c and d) LAI, under different SZA (0°, 15°, 30°, and 45°) using various reference bands (λ_{ref}) in the $SIPI_{\lambda_{ref}}$ [λ_1, λ_2] and $mND_{\lambda_{ref}}$ [λ_1, λ_2] format, In (a and c), the index calculation strategy is Ref_AVG. In (b and d), the index calculation strategy is Index_AVG. These results were obtained at 0.1-m spatial resolution and 2-nm spectral resolution.

influence [34], [35], [36], [52], [53]. Previous articles have suggested using entire-crown pixels for LAI estimation, as it produces the lowest correlation with C_{ab} and the highest correlation with LAI [14], [36]. This is in line with the current study, which demonstrates that using crown pixels can achieve the highest correlation between LAI and NBIs across the reference wavelengths (Fig. 4). However, this article also reveals that pixel selection for LAI estimation is complex; it depends on

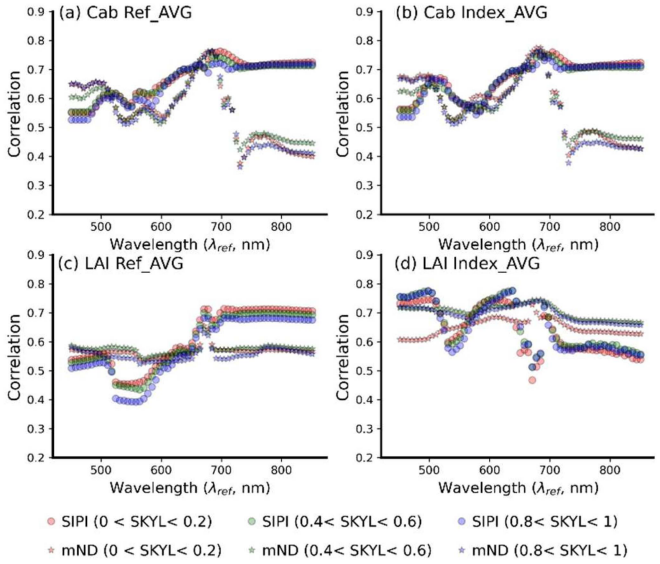

Fig. 9. Maximum Spearman's correlation coefficient values between NBIs and (a and b) C_{ab}, as well as (c and d) LAI, under different SKYL ($0 < SKYL < 0.2$, $0.4 < SKYL < 0.6$, $0.8 < SKYL < 1.0$) using various reference bands (λ_{ref}) in the $SIPI_{\lambda_{ref}}$ [λ_1, λ_2] and $mND_{\lambda_{ref}}$ [λ_1, λ_2] format. In (a and c), the index calculation strategy is Ref_AVG. In (b and d), the index calculation strategy is Index_AVG. The spatial resolution was 0.1 m and the spectral resolution was 2 nm.

the chosen reference wavelength, index calculation strategy, and spatial resolution of the images. The entire-crown pixels outperform others for reference wavelengths shorter than 700 nm using the Index_AVG strategy and longer than 700 nm using the Ref_AVG strategy (Fig. 4). The advantage of using the entire-crown for LAI estimation diminishes when using other reference wavelengths and index calculation strategies, and also decreases as spatial resolution decreases (Fig. 6).

This article demonstrates that the Ref_AVG and Index_AVG index calculation strategies yield similar correlations between NBIs and C_{ab} for spatial resolutions of 0.1, 0.5, 1, and 2 m (Fig. 5). This finding is consistent with a previous article, which indicated that these two strategies produce highly comparable results when the spatial resolution exceeds 10 cm [14]. Regarding LAI estimation, this article highlights the superiority of the Index_AVG strategy for reference bands below 650 nm, while both strategies demonstrate comparable performance for reference bands exceeding 700 nm (Fig. 4).

B. Spatial and Spectral Selection

Determining the optimal spatial resolution is crucial for enhancing parameter estimation accuracy without introducing noise and increasing computational burden. A previous article revealed that LAI estimation performances of hyperspectral images for sugar beet crops remained consistent for spatial resolutions finer than 4.4 cm but degraded with coarser resolutions [14]. Similarly, this article on urban trees demonstrates minimal differene in the estimate of C_{ab} for spatial resolutions finer than 1 m but a significant deterioration at 2-m resolution [Fig. 5(a) and (b)]. This indicates that a spatial resolution smaller than 2 m is optimal for C_{ab} estimation. For LAI estimation, 0.1-m resolution significantly outperforms coarser resolutions [0.5,

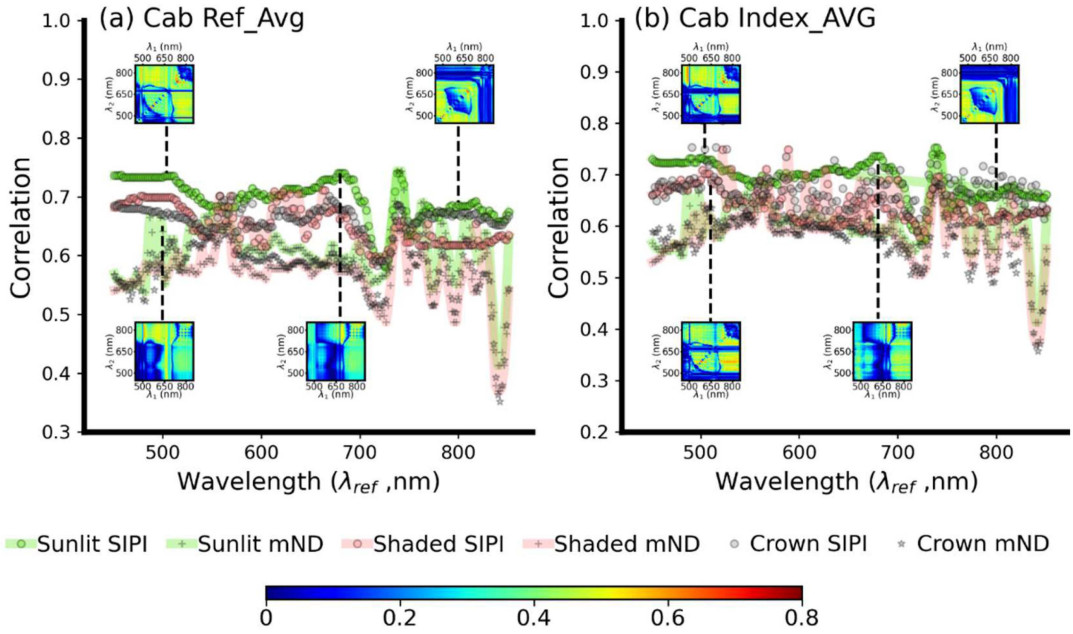

Fig. 10. Maximum Spearman's correlation coefficient values between NBIs derived from UAV hyperspectral images and C_{ab} using various reference bands (λ_{ref}) in the $SIPI_{\lambda_{ref}}$ [λ_1, λ_2], and $mND_{\lambda_{ref}}$ [λ_1, λ_2] format from sunlit, shaded, and entire crown pixels at 0.1-m spatial resolution. (a) Ref_AVG strategy. (b) Index_AVG strategy. The subfigure demonstrates the heat map of squared Spearman's correlation as a function of λ_1 and λ_2 wavebands with corresponding reference bands.

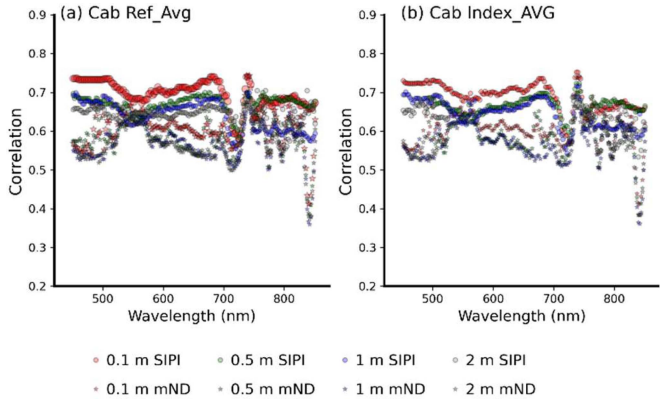

Fig. 11. Maximum Spearman's correlation coefficient values between NBIs derived from UAV hyperspectral images and C_{ab}, utilizing various reference bands (λ_{ref}) in the $SIPI_{\lambda_{ref}}$ [λ_1, λ_2] and $mND_{\lambda_{ref}}$ [λ_1, λ_2] format, with different spatial resolutions (0.1, 0.5, 1, and 2 m). Panels (a) use Ref_AVG strategy, while panels (b) use the Index_AVG strategy. The spectral resolution employed is 2 nm.

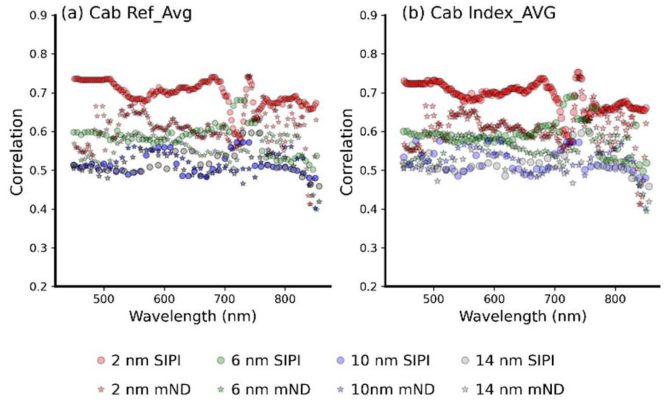

Fig. 12. Maximum Spearman's correlation coefficient values between NBIs derived from UAV hyperspectral images and C_{ab} for different spectral resolutions (2, 6, 10, and 14 nm), using various reference bands (λ_{ref}) in the $SIPI_{\lambda_{ref}}$ [λ_1, λ_2] and $mND_{\lambda_{ref}}$ [λ_1, λ_2] format. In (a), the index calculation strategy is Ref_AVG. In (b), the index calculation strategy is Index_AVG. The spatial resolution utilized was 0.1 m.

1, and 2 m; Fig. 5(c) and (d)], indicating that 0.1-m spatial resolution is optimal for LAI estimation. This suggests that current operational satellites, such as WorldView and Planet with resolutions of 2 and 3 m, respectively, may still be limited by their spatial resolution for LAI estimation. Thus, LAI estimates from UAVs could potentially serve as a reference for those derived from these satellite images. For accurate LAI estimation, UAVs must sacrifice flight efficiency by flying at lower altitudes and slower speeds to achieve higher spatial resolutions, ideally finer than 1 m for effective tree monitoring. In contrast, for C_{ab} estimation, UAVs can operate at higher altitudes and faster speeds, enhancing flight efficiency without significantly compromising the accuracy of C_{ab} measurements.

The 2-nm spectral resolution offers a significant advantage over coarser resolutions (6, 10, and 14 nm) for C_{ab} estimation for both index calculation strategies [Fig. 7(a) and (b)]. Even though previous articles show that LAI estimation from broadband indices can be influenced by illumination geometry, canopy architecture, leaf biochemistry, and background [51], this article shows that the impact of spectral resolution on LAI estimation is relatively minor, particularly when utilizing the Index_AVG strategy [Fig. (c) and (d)]. These findings could serve as a theoretical basis for sensor development aimed at C_{ab} and LAI estimation. For instance, cameras intended for tree C_{ab} estimation should prioritize higher spectral resolution, exceeding 2 nm, whereas for LAI estimation, the need for high spectral

resolution can be relaxed without significantly compromising accuracy, allowing for more cost-effective sensor options.

This article explores equal increments of spectral resolution for all wavelengths. However, some satellite missions increase the spectral resolution in certain spectral ranges. For example, several narrow waveband multispectral satellite sensors (e.g., RapidEye, Worldview-2, MERIS, and SumbandilaSAT) have been designed to include off-chlorophyll absorption center wavebands, which provide more sensitivity toward canopy biochemical constituents by including red-edge wavebands (i.e., 690–730 nm), while maintaining the characteristics (wider swaths, medium-to-high spatial resolutions, etc.) of multispectral sensors. The conclusions of this article also apply to such sensors when these specific wavelengths are used.

C. SZA and Illumination Selection

Previous article has demonstrated that oblique measurements are more sensitive to leaf properties compared to nadir measurements [48], [53], [54]. This increased sensitivity is attributed to a greater proportion of vegetation captured by the sensor and a reduced fraction of soil, resulting in a higher fraction of photons interacting with leaves before reaching the sensor. The current article supports these findings, revealing a stronger correlation between NBIs and C_{ab} at higher SZAs, implying that oblique SZAs are more effective for C_{ab} estimation [Fig. 8(a) and (b)]. In contrast, LAI, a structural characteristic of trees, exhibits a stronger correlation with NBIs when observed from a nadir view [Fig. 8(c) and (d)]. The variability in the correlation between NBIs and C_{ab} and LAI is partly due to the impact of anisotropic reflectance on spectral indices [55]. Notably, this article focuses exclusively on the influence of SZA, given the predominant nadir VZA of the UAV. Due to the Helmholtz reciprocity of the bidirectional reflectance distribution function, the effect of the VZA is expected to be similar to SZA in C_{ab} and LAI estimation. Consequently, our results align with those of previous articles indicating that nadir and oblique measurements are more sensitive to canopy structure and leaf biochemistry, respectively [48], [56].

Illumination also exhibits high variability and index-dependent effects on spectral indices. Therefore, careful consideration must be given to NBI selection to ensure that the interpretations are related to biophysical/biochemical phenomena rather than the effects of illumination [35]. Additionally, the impact of illumination on the correlation between NBIs and C_{ab} and LAI depends not only on the NBI format but also on the index calculation strategy (Fig. 9). Regarding the hypothesis that diffuse illumination conditions may have advantages in revealing spectral features in vegetation [35], this article shows the illumination barely influence C_{ab} estimation. However, for LAI estimation, the impact depends on the index calculation strategy used. Using Index_AVG calculation strategy, diffuse illumination benefits LAI estimation. Conversely, with the Ref_AVG calculation strategy, direct dominant illumination is more advantageous than diffuse illumination (Fig. 9). These findings indicate that the optimal image acquisition time for C_{ab} estimation is during early morning or late afternoon when the SZA is low, whereas for LAI estimation, local noon with a high SZA is more suitable. Weather conditions, such as clear or cloudy skies, do not significantly affect C_{ab} estimation. However, index calculation strategies should be adjusted according to varying illumination conditions for LAI estimation.

D. Differences and Limitations of Simulation and Field Data

The largest discrepancies between the simulation data profiles (Figs. 4, 5, and 7–9) and field data profiles (Figs. 10–12) in terms of maximum correlation between NBIs and C_{ab} occur in the blue band (450–500 nm) and a small portion of the NIR band (750–760 nm). Both ranges exhibit higher correlations in the field data than in the simulated results. This discrepancy may be due to greater atmospheric variability in the simulation data compared to UAV hyperspectral imagery. The sensitivity of indices utilizing the blue band (450–500 nm) and the oxygen absorption band (around 760 nm) to illumination conditions likely reduces the correlation with C_{ab}. Aside from these two ranges, the profiles of maximum correlation between NBIs and C_{ab} are consistent between the field and simulated data, with correlations increasing from 550 nm to a peak around 700 nm, followed by a stable lower plateau in the NIR band (770–850 nm).

Unfortunately, LAI field data were not collected simultaneously with the hyperspectral image acquisition, making it impossible to evaluate the simulation-derived conclusions regarding LAI. Additionally, exploring the influence of SZA and illumination on C_{ab} and LAI estimation using field data is challenging, as acquiring UAV hyperspectral images under varying SZA and weather conditions is difficult due to airspace restrictions and the unpredictability of the weather. Fortunately, the key strengths of radiative transfer model simulations is their ability to reveal new insights or patterns when remote sensing imagery and field measurements are unavailable. For instance, simulated images have been generated prior to the launch of new satellites to explore the ablility of the satellite images for parameter estimation [57], [58], [59], [60], [61], [62], [63] and radiative transfer model simulations have been used to evaluate field measurement methods when field data are lacking [43], [64]. In this article, the consistency between the simulation and field results for C_{ab} suggests that the model settings accurately represent urban environments, and the conclusions regarding LAI, SZA, and illumination drawn from the simulations are reliable.

Results derived from UAV hyperspectral images and field measurements (Figs. 4, 5, and 7–9) contain more outliers compared to the simulation data (Figs. 10–12). While field measurements are crucial for validating simulation settings, model simulations offer distinct advantages by providing controlled environments, avoiding confounding factors, such as camera noise, environmental noise during image acquisition (e.g., wind or atmospheric conditions), postprocessing inaccuracies (e.g., geolocation errors), and uncertainties in C_{ab} estimation during field measurements. Extracting meaningful information from the less noisy simulation data can be significantly more straightforward.

V. Conclusion

This article investigates the influence of observation configuration on the estimation of C_{ab} and LAI using NBIs derived from simulated hyperspectral images of trees generated by the 3-D

radiative transfer model, DART. The configurations considered include spatial resolution, spectral resolution, SZA, and SKYL. Additionally, this article examines the effectiveness of different index calculation strategies for C_{ab} and LAI estimation with sunlit, shaded, and entire-crown pixels. The findings reveal that, regardless of the index calculation strategy demployed, the sunlit pixels consistently outperform the shaded and entire-crown pixels for C_{ab} estimation across different spatial resolutions, including the 2-m spatial resolution. The strongest correlation is achieved when the reference band is around 700 nm. However, for LAI estimation, the highest correlation is observed when using entire-crown pixels with reference bands around 400–500 and 600–650 nm. The C_{ab} estimation is minimally affected by variations in spatial resolution, whereas LAI estimation is sensitive to spatial variations. A 0.1-m spatial resolution offers substantial advantages over coarser spatial resolutions for LAI estimation. Moreover, the advantages of using entire-crown pixels for LAI estimation diminish as spatial resolution decreases, while sunlit pixels exhibit stable correlations across different spatial resolutions. Higher spectral resolution (2 nm) significantly enhances C_{ab} estimation compared to coarser spectral resolutions (6, 10, and 14 nm), with smaller differences observed among these coarser spectral resolutions. LAI estimation appears less sensitive to changes in spectral resolution. In terms of SZA, an oblique SZA (45°) yields slightly higher correlations than a nadir SZA (0°) for C_{ab} estimation, whereas nadir SZA performs better for LAI estimation. The influence of the SKYL is minimal on C_{ab} estimation, but for LAI estimation, direct-dominant illumination performs slightly better with the Ref_AVG calculation strategy, while diffuse-dominant illumination performs slightly better with the Index_AVG calculation strategy. The exploration of the influence of spatial and spectral resolution on C_{ab} estimation using UAV hyperspectral images and field-measured C_{ab} demonstrates findings consistent with those derived from simulation data. This confirms the reliability of applying conclusions from the radiative transfer model to real-world scenarios, which is valuable for understanding the theory without direct measurements. This article provides valuable insights into the critical factors affecting hyperspectral image data for C_{ab} and LAI estimation. Such understanding is essential for enhancing vegetation monitoring using UAV data and guiding the development of future satellite missions.

Acknowledgment

The authors would like to thank the DART group, particularly Jean-Philippe Gastellu-Etchegorry and Nicolas Lauret, at the Centre d'Études Spatiales de la BIOsphère—UPS, CNES, CNRS, IRD, Université de Toulouse, for their support. We also extend our gratitude to all those who provided invaluable comments on this article.

References

[1] D. E. Bowler, L. Buyung-Ali, T. M. Knight, and A. S. Pullin, "Urban greening to cool towns and cities: A systematic review of the empirical evidence," *Landscape Urban Plan.*, vol. 97, no. 3, pp. 147–155, 2010, doi: 10.1016/j.landurbplan.2010.05.006.

[2] J. Yang, Y. Chang, and P. Yan, "Ranking the suitability of common urban tree species for controlling PM2.5 pollution," *Atmospheric Pollut. Res.*, vol. 6, no. 2, pp. 267–277, 2015, doi: 10.5094/APR.2015.031.

[3] Z. G. Davies, J. L. Edmondson, A. Heinemeyer, J. R. Leake, and K. J. Gaston, "Mapping an urban ecosystem service: Quantifying above-ground carbon storage at a city-wide scale," *J. Appl. Ecol.*, vol. 48, no. 5, pp. 1125–1134, Oct. 2011, doi: 10.1111/j.1365-2664.2011.02021.x.

[4] A. Berland and M. E. Hopton, "Comparing street tree assemblages and associated stormwater benefits among communities in metropolitan Cincinnati, Ohio, USA," *Urban Forest Urban Green*, vol. 13, no. 4, pp. 734–741, 2014, doi: 10.1016/j.ufug.2014.06.004.

[5] K. Buonasera, M. Lambreva, G. Rea, E. Touloupakis, and M. T. Giardi, "Technological applications of chlorophyll a fluorescence for the assessment of environmental pollutants.," *Anal. Bioanal. Chem.*, vol. 401, no. 4, pp. 1139–1151, Sep. 2011, doi: 10.1007/s00216-011-5166-1.

[6] Z. Malenovský et al., "Retrieval of spruce leaf chlorophyll content from airborne image data using continuum removal and radiative transfer," *Remote Sens. Environ.*, vol. 131, pp. 85–102, Apr. 2013, doi: 10.1016/j.rse.2012.12.015.

[7] I. Olthof, D. J. King, and R. A. Lautenschlager, "Overstory and understory leaf area index as indicators of forest response to ice storm damage," *Ecol. Indicators*, vol. 3, no. 1, pp. 49–64, Apr. 2003, doi: 10.1016/S1470-160X(03)00010-4.

[8] I. Olthof, D. J. King, and R. A. Lautenschlager, "Leaf area index change in ice-storm-damaged sugar maple stands," *Forest Chronicle*, vol. 77, no. 4, pp. 627–635, Aug. 2001, doi: 10.5558/tfc77627-4.

[9] T. Manninen, P. Stenberg, M. Rautiainen, and P. Voipio, "Leaf area index estimation of boreal and subarctic forests using VV/HH ENVISAT/ASAR data of various swaths," *IEEE Trans. Geosci. Remote Sens.*, vol. 51, no. 7, pp. 3899–3909, Jul. 2013, doi: 10.1109/TGRS.2012.2227327.

[10] I. Barka et al., "Remote sensing-based forest health monitoring systems—Case studies from Czechia and Slovakia," *Central Eur. Forestry J.*, vol. 64, no. 3–4, pp. 259–275, 2018, doi: 10.1515/forj-2017-0051.

[11] J. Degerickx, D. A. Roberts, J. P. McFadden, M. Hermy, and B. Somers, "Urban tree health assessment using airborne hyperspectral and LiDAR imagery," *Int. J. Appl. Earth Observ. Geoinf.*, vol. 73, pp. 26–38, Dec. 2018, doi: 10.1016/j.jag.2018.05.021.

[12] D. Haboudane, J. R. Miller, N. Tremblay, P. J. Zarco-Tejada, and L. Dextraze, "Integrated narrow-band vegetation indices for prediction of crop chlorophyll content for application to precision agriculture," *Remote Sens. Environ.*, vol. 81, no. 2, pp. 416–426, Aug. 2002, doi: 10.1016/S0034-4257(02)00018-4.

[13] P. J. Zarco-Tejada, J. R. Miller, A. Morales, A. Berjón, and J. Agüera, "Hyperspectral indices and model simulation for chlorophyll estimation in open-canopy tree crops," *Remote Sens. Environ.*, vol. 90, no. 4, pp. 463–476, Apr. 2004, doi: 10.1016/j.rse.2004.01.017.

[14] S. Jay et al., "Estimating leaf chlorophyll content in sugar beet canopies using millimeter- to centimeter-scale reflectance imagery," *Remote Sens. Environ.*, vol. 198, pp. 173–186, Sep. 2017, doi: 10.1016/j.rse.2017.06.008.

[15] R. Colombo, D. Bellingeri, D. Fasolini, and C. M. Marino, "Retrieval of leaf area index in different vegetation types using high resolution satellite data," *Remote Sens. Environ.*, vol. 86, no. 1, pp. 120–131, Jun. 2003, doi: 10.1016/S0034-4257(03)00094-4.

[16] W. Laongmanee, "Assessment of spatial resolution in estimating leaf area index from satellite images: A case study with Avicennia marina plantations in Thailand," *Int. J. Geoinformatics*, vol. 9, pp. 69–77, 2013. [Online]. Available: https://api.semanticscholar.org/CorpusID:129075719

[17] M. Sprintsin, A. Karnieli, P. Berliner, E. Rotenberg, D. Yakir, and S. Cohen, "The effect of spatial resolution on the accuracy of leaf area index estimation for a forest planted in the desert transition zone," *Remote Sens. Environ.*, vol. 109, no. 4, pp. 416–428, Aug. 2007, doi: 10.1016/j.rse.2007.01.020.

[18] C. Wu, Z. Niu, Q. Tang, and W. Huang, "Estimating chlorophyll content from hyperspectral vegetation indices: Modeling and validation," *Agricultural Forest Meteorol.*, vol. 148, no. 8, pp. 1230–1241, Jul. 2008, doi: 10.1016/j.agrformet.2008.03.005.

[19] D. Gao et al., "Improvement of chlorophyll content estimation on maize leaf by vein removal in hyperspectral image," *Comput. Electron. Agriculture*, vol. 184, May 2021, Art. no. 106077, doi: 10.1016/j.compag.2021.106077.

[20] D. Haboudane, N. Tremblay, J. R. Miller, and P. Vigneault, "Remote estimation of crop chlorophyll content using spectral indices derived from hyperspectral data," *IEEE Trans. Geosci. Remote Sens.*, vol. 46, no. 2, pp. 423–437, Feb. 2008, doi: 10.1109/TGRS.2007.904836.

[21] J. Delegido, L. Alonso, G. Gonzalez, and J. Moreno, "Estimating chlorophyll content of crops from hyperspectral data using a normalized area over reflectance curve (NAOC)," *Int. J. Appl. Earth Observ. Geoinf.*, vol. 12, no. 3, pp. 165–174, 2010.

[22] M. Vincini, E. Frazzi, and P. D'Alessio, "A broad-band leaf chlorophyll vegetation index at the canopy scale," *Precis. Agriculture*, vol. 9, no. 5, pp. 303–319, Oct. 2008, doi: 10.1007/s11119-008-9075-z.

[23] X. Li and A. H. Strahler, "Geometric-optical modeling of a conifer forest canopy," *IEEE Trans. Geosci. Remote Sens.*, vol. GE-23, no. 5, pp. 705–721, Sep. 1985, doi: 10.1109/TGRS.1985.289389.

[24] J. M. Chen and S. G. Leblanc, "A four-scale bidirectional reflectance model based on canopy architecture," *IEEE Trans. Geosci. Remote Sens.*, vol. 35, no. 5, pp. 1316–1337, Sep. 1997, doi: 10.1109/36.628798.

[25] M. Vincini, F. Calegari, and R. Casa, "Sensitivity of leaf chlorophyll empirical estimators obtained at Sentinel-2 spectral resolution for different canopy structures," *Precis. Agriculture*, vol. 17, no. 3, pp. 313–331, Jun. 2016, doi: 10.1007/s11119-015-9424-7.

[26] M. Vincini, S. Amaducci, and E. Frazzi, "Empirical estimation of leaf chlorophyll density in winter wheat canopies using Sentinel-2 spectral resolution," *IEEE Trans. Geosci. Remote Sens.*, vol. 52, no. 6, pp. 3220–3235, Jun. 2014.

[27] H. Croft, J. Arabian, J. M. Chen, J. Shang, and J. Liu, "Mapping within-field leaf chlorophyll content in agricultural crops for nitrogen management using Landsat-8 imagery," *Precis. Agriculture*, vol. 21, no. 4, pp. 856–880, Aug. 2020, doi: 10.1007/s11119-019-09698-y.

[28] J. M. Chen and S. G. Leblanc, "A four-scale bidirectional reflectance model based on canopy architecture," *IEEE Trans. Geosci. Remote Sens.*, vol. 35, no. 5, pp. 1316–1337, Sep. 1997.

[29] X. Li and A. H. Strahler, "Geometric-optical modeling of a conifer forest canopy," *IEEE Trans. Geosci. Remote Sens.*, no. 5, pp. 705–721, 1985.

[30] P. J. Zarco-Tejada, J. R. Miller, T. L. Noland, G. H. Mohammed, and P. H. Sampson, "Scaling-up and model inversion methods with narrowband optical indices for chlorophyll content estimation in closed forest canopies with hyperspectral data," *IEEE Trans. Geosci. Remote Sens.*, vol. 39, no. 7, pp. 1491–1507, Jul. 2001, doi: 10.1109/36.934080.

[31] P. J. Zarco-Tejada, M. L. Guillén-Climent, R. Hernández-Clemente, A. Catalina, M. R. González, and P. Martín, "Estimating leaf carotenoid content in vineyards using high resolution hyperspectral imagery acquired from an unmanned aerial vehicle (UAV)," *Agricultural Forest Meteorol.*, vol. 171–172, pp. 281–294, 2013, doi: 10.1016/j.agrformet.2012.12.013.

[32] U. Heiden, K. Segl, S. Roessner, and H. Kaufmann, "Determination of robust spectral features for identification of urban surface materials in hyperspectral remote sensing data," *Remote Sens. Environ.*, vol. 111, no. 4, pp. 537–552, Dec. 2007, doi: 10.1016/j.rse.2007.04.008.

[33] D. Li et al., "Improved estimation of leaf chlorophyll content of row crops from canopy reflectance spectra through minimizing canopy structural effects and optimizing off-noon observation time," *Remote Sens. Environ.*, vol. 248, Oct. 2020, Art. no. 111985, doi: 10.1016/j.rse.2020.111985.

[34] M. P. Ferreira et al., "Retrieving structural and chemical properties of individual tree crowns in a highly diverse tropical forest with 3D radiative transfer modeling and imaging spectroscopy," *Remote Sens. Environ.*, vol. 211, pp. 276–291, Jun. 2018, doi: 10.1016/j.rse.2018.04.023.

[35] J. P. Arroyo-Mora et al., "Assessing the impact of illumination on UAV pushbroom hyperspectral imagery collected under various cloud cover conditions," *Remote Sens. Environ.*, vol. 258, Jun. 2021, Art. no. 112396, doi: 10.1016/j.rse.2021.112396.

[36] S. Wei et al., "Estimation of chlorophyll content for urban trees from UAV hyperspectral images," *Int. J. Appl. Earth Observ. Geoinf.*, vol. 126, Feb. 2024, Art. no. 103617, doi: 10.1016/j.jag.2023.103617.

[37] J.-B. Féret, K. Berger, F. de Boissieu, and Z. Malenovský, "PROSPECT-PRO for estimating content of nitrogen-containing leaf proteins and other carbon-based constituents," *Remote Sens. Environ.*, vol. 252, 2021, Art. no. 112173, doi: 10.1016/j.rse.2020.112173.

[38] J.-B. Feret et al., "PROSPECT-4 and 5: Advances in the leaf optical properties model separating photosynthetic pigments," *Remote Sens. Environ.*, vol. 112, no. 6, pp. 3030–3043, 2008, doi: 10.1016/j.rse.2008.02.012.

[39] J.-P. Gastellu-Etchegorry et al., "Discrete anisotropic radiative transfer (DART 5) for modeling airborne and satellite spectroradiometer and LiDAR acquisitions of natural and urban landscapes," *Remote Sens.*, vol. 7, no. 2, pp. 1667–1701, 2015, doi: 10.3390/rs70201667.

[40] J. Gastellu-Etchegorry et al., "DART: Recent advances in remote sensing data modeling with atmosphere, polarization, and chlorophyll fluorescence," *IEEE J. Sel. Top. Appl. Earth Observ. Remote Sens.*, vol. 10, no. 6, pp. 2640–2649, Jun. 2017, doi: 10.1109/JSTARS.2017.2685528.

[41] J. P. Gastellu-Etchegorry, V. Demarez, V. Pinel, and F. Zagolski, "Modeling radiative transfer in heterogeneous 3-D vegetation canopies," *Remote Sens. Environ.*, vol. 58, no. 2, pp. 131–156, 1996, doi: 10.1016/0034-4257(95)00253-7.

[42] J. P. Gastellu-Etchegorry, E. Martin, and F. Gascon, "DART: A 3D model for simulating satellite images and studying surface radiation budget," *Int. J. Remote Sens.*, vol. 25, no. 1, pp. 73–96, Jan. 2004, doi: 10.1080/0143116031000115166.

[43] S. Wei et al., "An assessment study of three indirect methods for estimating leaf area density and leaf area index of individual trees," *Agricultural Forest Meteorol.*, vol. 292–293, Oct. 2020, Art. no. 108101, doi: 10.1016/j.agrformet.2020.108101.

[44] T. Yun et al., "Status, advancements and prospects of deep learning methods applied in forest studies," *Int. J. Appl. Earth Observ. Geoinf.*, vol. 131, Jul. 2024, Art. no. 103938, doi: 10.1016/j.jag.2024.103938.

[45] T. Zhao et al., "Artificial intelligence for geoscience: Progress, challenges, and perspectives," *Innovation*, vol. 5, no. 5, Sep. 2024, Art. no. 100691, doi: 10.1016/j.xinn.2024.100691.

[46] M. Kalacska, M. Lalonde, and T. R. Moore, "Estimation of foliar chlorophyll and nitrogen content in an ombrotrophic bog from hyperspectral data: Scaling from leaf to image," *Remote Sens. Environ.*, vol. 169, pp. 270–279, Nov. 2015, doi: 10.1016/j.rse.2015.08.012.

[47] A. Tong and Y. He, "Estimating and mapping chlorophyll content for a heterogeneous grassland: Comparing prediction power of a suite of vegetation indices across scales between years," *ISPRS J. Photogrammetry Remote Sens.*, vol. 126, pp. 146–167, Apr. 2017, doi: 10.1016/j.isprsjprs.2017.02.010.

[48] S. Jay, F. Maupas, R. Bendoula, and N. Gorretta, "Retrieving LAI, chlorophyll and nitrogen contents in sugar beet crops from multi-angular optical remote sensing: Comparison of vegetation indices and PROSAIL inversion for field phenotyping," *Field Crops Res.*, vol. 210, pp. 33–46, Aug. 2017, doi: 10.1016/j.fcr.2017.05.005.

[49] S. Jay et al., "Exploiting the centimeter resolution of UAV multispectral imagery to improve remote-sensing estimates of canopy structure and biochemistry in sugar beet crops," *Remote Sens. Environ.*, vol. 231, Sep. 2019, Art. no. 110898, doi: 10.1016/j.rse.2018.09.011.

[50] I. Moorthy, J. R. Miller, and T. L. Noland, "Estimating chlorophyll concentration in conifer needles with hyperspectral data: An assessment at the needle and canopy level," *Remote Sens. Environ.*, vol. 112, no. 6, pp. 2824–2838, Jun. 2008, doi: 10.1016/J.RSE.2008.01.013.

[51] N. H. Broge and E. Leblanc, "Comparing prediction power and stability of broadband and hyperspectral vegetation indices for estimation of green leaf area index and canopy chlorophyll density," *Remote Sens. Environ.*, vol. 76, no. 2, pp. 156–172, May 2001, doi: 10.1016/S0034-4257(00)00197-8.

[52] F. Baret, B. de Solan, R. Lopez-Lozano, K. Ma, and M. Weiss, "GAI estimates of row crops from downward looking digital photos taken perpendicular to rows at 57.5° zenith angle: Theoretical considerations based on 3D architecture models and application to wheat crops," *Agricultural Forest Meteorol.*, vol. 150, no. 11, pp. 1393–1401, Oct. 2010, doi: 10.1016/j.agrformet.2010.04.011.

[53] S. Jacquemoud et al., "PROSPECT+SAIL models: A review of use for vegetation characterization," *Remote Sens. Environ.*, vol. 113, pp. S56–S66, Sep. 2009, doi: 10.1016/j.rse.2008.01.026.

[54] W. A. Dorigo, "Improving the robustness of cotton status characterisation by radiative transfer model inversion of multi-angular CHRIS/PROBA data," *IEEE J. Sel. Top. Appl. Earth Observ. Remote Sens.*, vol. 5, pp. 18–29, 2012.

[55] C. A. Coburn, E. V. Gaalen, D. R. Peddle, and L. B. Flanagan, "Anisotropic reflectance effects on spectral indices for estimating ecophysiological parameters using a portable goniometer system," *Can. J. Remote Sens.*, vol. 36, pp. S355–S364, Jan. 2010, doi: 10.5589/m10-066.

[56] L. He et al., "Comparing methods for estimating leaf area index by multi-angular remote sensing in winter wheat.," *Sci. Rep.*, vol. 10, no. 1, Aug. 2020, Art. no. 13943, doi: 10.1038/s41598-020-70951-w.

[57] C. Gomez, R. Oltra-Carrió, S. Bacha, P. Lagacherie, and X. Briottet, "Evaluating the sensitivity of clay content prediction to atmospheric effects and degradation of image spatial resolution using hyperspectral VNIR/SWIR imagery," *Remote Sens. Environ.*, vol. 164, pp. 1–15, Jul. 2015, doi: 10.1016/j.rse.2015.02.019.

[58] A. Okujeni, S. van der Linden, and P. Hostert, "Extending the vegetation–impervious–soil model using simulated EnMAP data and machine learning," *Remote Sens. Environ.*, vol. 158, pp. 69–80, Mar. 2015, doi: 10.1016/j.rse.2014.11.009.

[59] M. Locherer, T. Hank, M. Danner, and W. Mauser, "Retrieval of seasonal leaf area index from simulated EnMAP data through optimized LUT-based inversion of the PROSAIL model," *Remote Sens.*, vol. 7, no. 8, pp. 10321–10346, 2015, doi: 10.3390/rs70810321.
[60] M. Schwieder, P. J. Leitão, S. Suess, C. Senf, and P. Hostert, "Estimating fractional shrub cover using simulated EnMAP data: A comparison of three machine learning regression techniques," *Remote Sens.*, vol. 6, no. 4, pp. 3427–3445, 2014, doi: 10.3390/rs6043427.
[61] S. Cooper, A. Okujeni, C. Jänicke, M. Clark, S. van der Linden, and P. Hostert, "Disentangling fractional vegetation cover: Regression-based unmixing of simulated spaceborne imaging spectroscopy data," *Remote Sens. Environ.*, vol. 246, 2020, Art. no. 111856.
[62] A. Okujeni et al., "Multi-season unmixing of vegetation class fractions across diverse Californian ecoregions using simulated spaceborne imaging spectroscopy data," *Remote Sens. Environ.*, vol. 264, 2021, Art. no. 112558.
[63] A. Marcinkowska-Ochtyra et al., "Subalpine and alpine vegetation classification based on hyperspectral APEX and simulated EnMAP images," *Int. J. Remote Sens.*, vol. 38, no. 7, pp. 1839–1864, 2017.
[64] E. Grau, S. Durrieu, R. Fournier, J.-P. Gastellu-Etchegorry, and T. Yin, "Estimation of 3D vegetation density with terrestrial laser scanning data using voxels: A sensitivity analysis of influencing parameters," *Remote Sens. Environ.*, vol. 191, pp. 373–388, Mar. 2017, doi: 10.1016/j.rse.2017.01.032.

Shanshan Wei received the B.Sc. degree in cartography and geographic information systems from the Department of Geography, School of Urban and Environmental Sciences, Northeast Normal University, Changchun, China, in 2008, the second B.Sc. degree in computer science from the College of Software, Northeast Normal University, in 2009, and the Ph.D. degree in cartography and geographic information systems from the Institute of Geographic Sciences and Natural Resources Research, University of Chinese Academy of Sciences, Beijing, China, in 2017.

From 2017 to 2022, she was a Postdoctoral Researcher with the Singapore–MIT Alliance for Research and Technology. She is currently a Research Scientist with the Centre for Remote Imaging, Sensing and Processing, National University of Singapore, Singapore. She has reviewed more than 60 papers for 12 remote sensing journals and served as a Guest Editor for Remote Sensing and All Earth. Since 2021, she has been serving as a proposal Reviewer for the National Research Foundation, Singapore. Her research interests include estimating biophysical and biochemical parameters using satellite, UAV, and field data, as well as leaf-canopy radiative transfer models.

Tiangang Yin received the B.Sc. degree in physics and the M.Eng. degree in computer engineering from the National University of Singapore, Singapore, in 2008 and 2011, respectively, and the Ph.D. degree in remote sensing and geoscience from the Centre d'Etudes Spatiales de la BIOsphère, Paul Sabatier University, Toulouse, France, in 2015.

He is currently an Assistant Professor with the Department of Land Surveying and Geo-Informatics, the Hong Kong Polytechnic University, Hong Kong. Prior to joining the LSGI, he was a Research Scientist jointly with the NASA Goddard Space Flight Center and the Earth System Science Interdisciplinary Center, University of Maryland, College Park, MD, USA. Since 2012, he has been leading research and development of several modules (LiDAR, photogrammetry, and urban atmosphere) for the discrete anisotropic radiative transfer model.

Dr. Yin is serving as a member (director of research) for IEEE Geoscience and Remote Sensing Society—Hong Kong Chapter.

Bo Yuan received the B.Sc. and M.Sc. degrees in nuclear physics from the Peking University, Beijing, China, in 1985 and 1988, respectively, and the M.Sc. and Ph.D. degrees in computer science from the National University of Singapore, Singapore, in 2000 and 2006, respectively.

He has been working with the universities, research institutions, and commercial companies in the fields of information and remote sensing technologies for environmental and marine applications.

Kim Hwa Lim received the Ph.D. degree in electrical and computer engineering from the Duke University, Durham, NC, USA, in 2007.

He is currently the Deputy Director of the Centre for Remote Imaging Sensing and Processing (CRISP), NUS, Singapore. He has been working with the CRISP, since 2003, except for 2015–2020, he served as the Chief Technology Officer of a private company LightHaus Imaging Pte. Ltd. and cofound frinGOe Pte. Ltd.

Soo Chin Liew received the Ph.D. degree in physics from the University of Arizona, Tucson, AZ, USA, in 1989.

He is currently a Principal Research Scientist (rank of Associate Professor) and the Head of Research with the Center for Remote Imaging, Sensing and Processing, National University of Singapore (NUS), Singapore. He did postdoctoral research with the Physics Research Lab, University of California at San Francisco (UCSF) Radiology Department before joining the NUS. He has previous research experience in thermoacoustic emission, X-ray transmission and single photon emission computed tomography, nuclear microscopy, and image processing. His research interests include remote sensing of the Earth with expertise in hyperspectral imaging, ocean optics, inland and coastal water quality, atmospheric aerosols, forest fires, and land cover change.

Dr. Liew is an Associate Editor of *Frontiers in Remote Sensing*, Review Editor of *Frontiers in Environmental Science*, a member of the Editorial Board of *Remote Sensing*, and a former Associate Editor of *SPIE Journal of Applied Remote Sensing* (2014–2019). He participated as a PI in NASA EO-1 satellite science team working on the Hyperion instrument.

Andrew J. Whittle received the B.Sc. degree from the Imperial College, London, U.K., in 1981, and the Sc.D. degree from the MIT, Cambridge, MA, USA, in 1987, both in civil engineering.

He is the Edmund K. Turner of Civil & Environmental Engineering with the MIT. He has been a Faculty Member with the MIT for more than 35 years. He is an expert in geotechnical engineering, whose research deals principally with formulation of constitutive models for representing the complex mechanical properties of soils and their application in predicting the performance of constructed facilities. He served as lead PI for the SMART-Center for Environmental Sensing and Modeling in Singapore through which he has conducted research on a variety of environmental sensing projects, including city scale monitoring of water distribution systems, integrated monitoring and modeling for underground excavations and tunnels, and remote sensing for the management of urban trees.